HEALTH STRUCTURE MONITORING FOR AIRCRAFT AND ROTORCRAFT THROUGH INVERSE FINITE ELEMENT METHOD (IFEM)

U. Papa, S. Russo, and G. Iannuzzo
Leonardo Company – Aircraft Division
Viale dell'Aeronautica, 80038
Pomigliano d'Arco, Naples
Italy

ABSTRACT

Structural health monitoring (SHM) is an important task in system health management applications for aeronautic and space transportation vehicles, manned and unmanned. The rotorcraft are also extremely needed in various fields of interest, from military to civilian (search and rescue, environmental surveillance and monitoring, entertainment). This work presents an innovative structure design and control through an inverse finite element method-based, which compute the full-field displacements reconstruction of a three-dimensional shell/plate deformations from experimentally measured surface strains. The full-field displacements are useful for the preliminary design and inspections of the rotorcraft loads, caused by maneuvers or gusts. Goal of this paper was to validate the high accuracy predictions of deformations afforded due to the inverse finite element method (iFEM). Overall formulation was based on the minimization of a least-squares functional that uses and compares the strains extracted due to embedded sensors with the strains of linear, first order shear-deformation theory. The test article was a thin plate equipped with embedded sensors (strain gauge sensors) which permit to extract surface strains in real-time, used as input data for shape sensing. The plate was used to approximate a rotorcraft fuselage skin, in further work analyzed.

Keywords: Structural Health Monitoring, Rotorcraft/Aircraft Design; Finite Element Method; Inverse problem, Linear Deformation Theory.

1 INTRODUCTION

Advanced structural health monitoring is generally regarded as a vital technology for the next generation of aeronautical and space systems (Noor et al., 2000). Aim of the structural health monitoring (SHM) is to prevent and avoid fatal structural damages through the determination of stresses and deformations (i.e. displacements) of whole structure or a specific component. It is clear that external loads and boundary conditions should be previously identified.
The reconstruction of full-field structural displacements, i.e. shape sensing, and external loads will be one of major area of interest for structural real-time researches and analysis. Future aircraft will be equipped with a health monitoring and actuation control systems; for example, giving a feedback in real time in case of morphed-wing configuration in an space/aircraft or in an unmanned aircraft system (UAS). To make easy such capabilities, the load carrying structural components will be aided through a network of strain gauge sensors (SG) or fiber optic sensors (FOS).
Aim of this paper was to develop a finite element-based methodology (FEM) relating an inverse formulation which employs measured surface strains to recover the applied loads, stresses, and displacements on an aerospace

vehicle in real time. The determination of loads, stresses, and displacements, using experimentally measured structural response (strains rosette or fiber optic sensors), were defined as an inverse FEM problem (iFEM). This methodology (iFEM) uses a least-squares variational principle, which is discretized by C^0-*continous* inverse triangular elements.

The mathematical concepts applied in this paper may be found in Tichonov et al., 1977 and Tarantola, 1987, however the main equations used will be proposed in the following sections. Considering small changes in the acquired data, Tikhonov and Arsenin, 1977 formulated a method to have an approximate solution.

Recently, Shkarayev et al., 2001, Bogert et al., 2003, and Tessler and Spangler 1983 and 2005, using different least-squares approaches, focused on the inverse problem of reconstructing the three-dimensional displacements in plate and shell aerospace structures from in-situ strain-sensor measurements. Recent advances in the design of structural health monitoring (SHM) for aerospace applications are also discussed in Tessler and Spangler 2004 and 2005.

The present work merges and compares a computational mechanics methodology with experimentally measured strain data from strain gauges (SGs), strain rosettes or fiber optic sensors (FOSS), in manner to determine the in-flight response characteristics of a rotorcraft fuselage skin panel. The sensors were embedded in the considered structure along specified patterns, in this case the wingspan, giving strain component measurements at specific locations. The iFEM takes advantage to strain measurements in manner to reconstruct the deformed shape of the plate, which was used to make easier the wing-box section. This methodology was also applicable, for example, to an aircraft landing gear structure in order to obtain stress and displacements induced by shocks during landing procedure. This will be addressed in further works. The methodology compare the displacements obtained through to the classical FEM, performed in MSC/NASTRAN software, and the iFem algorithm, using Matlab environment. The wing box, as mentioned, will be reduced in an equivalent plate shells, considering the Mindlin plate approximation. The iFEM method do not provide the use of material property (e.g. Young or Poisson modulus) and loads. Details about the test article configuration and related experimental results are described. Conclusion and further works will be reported in the last section.

2 INVERSE FINITE ELEMENT METHOD (IFEM)

The iFEM was developed on triangular flat shell element, defined as iTRIA3 (Figure 1), where deformations were defined considering three components of the displacements vector $\boldsymbol{u}\ \{u, v, w, \theta_x, \theta_y\}^T$, in accordance to Mindlin theory (1951). This was defined in a three-dimensional Cartesian coordinate system (*x, y, z*) :

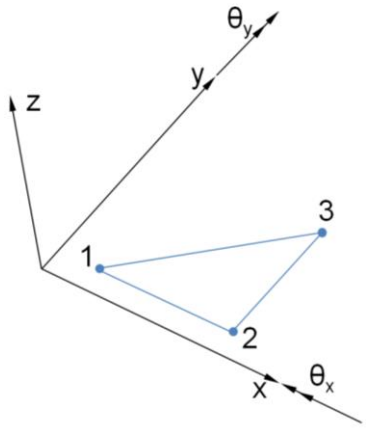

Figure 1. iTRIA3 inverse shell element, three nodes.

$$
\begin{aligned}
u_x(x,y,z) &= u + z\theta_y \\
u_y(x,y,z) &= v + z\theta_x \\
u_z(x,y,z) &= w
\end{aligned}
\qquad (1)
$$

The displacements along *x* and *y* axis, *u* and *v* defined in Eq. (1), will be considered at

the mid-plane and *w* will be the displacements, assumed constant, across the thickness range $z \in [-t, +t]$; considering the total shell thickness as *2t*. Instead, the rotations of the normal around *x* and *y* axes are respectively θ_x and θ_y.

The strain-displacement relations of linear elasticity theory, in *xy* plane (Noor 1974 and Zienkiewics 2000), by the subsequent system equations, were defined:

$$\begin{Bmatrix} \varepsilon_{xx} \\ \varepsilon_{yy} \\ \gamma_{xy} \end{Bmatrix} = \begin{Bmatrix} \varepsilon_{x0} \\ \varepsilon_{y0} \\ \gamma_{xy0} \end{Bmatrix} + z \begin{Bmatrix} \kappa_{x0} \\ \kappa_{y0} \\ \kappa_{xy0} \end{Bmatrix} \equiv e(u) + z\kappa(u) \tag{2}$$

Considering the five kinematic variables, equation above will be:

$$e(u) = \begin{Bmatrix} \varepsilon_{x0} \\ \varepsilon_{y0} \\ \gamma_{xy0} \end{Bmatrix} = \begin{bmatrix} \frac{\partial}{\partial x} & 0 & 0 & 0 & 0 \\ 0 & \frac{\partial}{\partial y} & 0 & 0 & 0 \\ \frac{\partial}{\partial y} & \frac{\partial}{\partial x} & 0 & 0 & 0 \end{bmatrix} \begin{Bmatrix} u \\ v \\ w \\ \theta_x \\ \theta_y \end{Bmatrix} \tag{3}$$

$$\kappa(u) = \begin{Bmatrix} \kappa_{x0} \\ \kappa_{y0} \\ \kappa_{xy0} \end{Bmatrix} = \begin{bmatrix} 0 & 0 & 0 & 0 & \frac{\partial}{\partial x} \\ 0 & 0 & 0 & \frac{\partial}{\partial y} & 0 \\ 0 & 0 & 0 & \frac{\partial}{\partial y} & \frac{\partial}{\partial x} \end{bmatrix} \begin{Bmatrix} u \\ v \\ w \\ \theta_x \\ \theta_y \end{Bmatrix} \tag{4}$$

Assuming that structure was instrumented with *N* strain sensors (e.g. strain gauge rosette or fiber-optic sensors), the strain were given by:

$$e_i^{\varepsilon} \equiv \begin{Bmatrix} \varepsilon_{x0}^{\varepsilon} \\ \varepsilon_{y0}^{\varepsilon} \\ \gamma_{xy0}^{\varepsilon} \end{Bmatrix}_i = \frac{1}{2} \left(\begin{Bmatrix} \varepsilon_{xx}^{+} \\ \varepsilon_{yy}^{+} \\ \gamma_{xy0}^{+} \end{Bmatrix}_i + \begin{Bmatrix} \varepsilon_{xx}^{-} \\ \varepsilon_{yy}^{-} \\ \gamma_{xy0}^{-} \end{Bmatrix}_i \right)$$

$$\kappa_i^{\varepsilon} \equiv \begin{Bmatrix} \kappa_{x0}^{\varepsilon} \\ \kappa_{y0}^{\varepsilon} \\ \kappa_{xy0}^{\varepsilon} \end{Bmatrix}_i = \frac{1}{2t} \left(\begin{Bmatrix} \varepsilon_{xx}^{+} \\ \varepsilon_{yy}^{+} \\ \gamma_{xy0}^{+} \end{Bmatrix}_i - \begin{Bmatrix} \varepsilon_{xx}^{-} \\ \varepsilon_{yy}^{-} \\ \gamma_{xy0}^{-} \end{Bmatrix}_i \right) \tag{5}$$

The subscript $i=1,N$ and superscript ε refer to the existence of an experimental error in strain measurements, thus in stretching of the middle surface ε and the bending curvatures κ . Thus, superscript "+" or "–", refers to SG position along the thickness, in detail "+" for on top SG positioning, vice versa for "–" sign (see Figure 2). The SG, in this

case, will be positioned in a *back-to-back* mode.

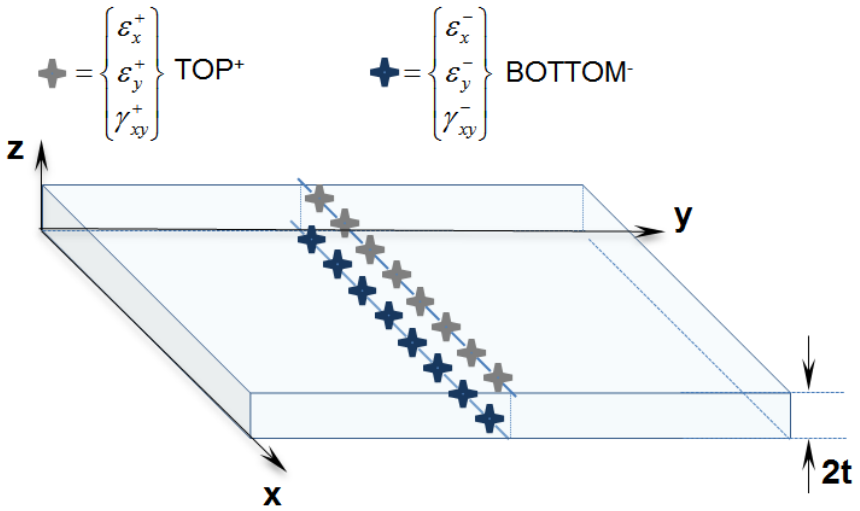

Figure 2. Strain gauges (SG) positioning.

Following Tessler and Spangler, 2004, the transverse shear strain *g(u)* was given by:

$$g(u) \equiv \{\gamma_{xz}, \gamma_{yz}\}^T$$

(6)
$$g(u) \equiv \begin{Bmatrix} \gamma_{xz0} \\ \gamma_{yz0} \end{Bmatrix} = \begin{bmatrix} 0 & 0 & \frac{\partial}{\partial x} & 0 & 1 \\ 0 & 0 & \frac{\partial}{\partial y} & 1 & 0 \end{bmatrix} \begin{Bmatrix} u \\ v \\ w \\ \theta_x \\ \theta_y \end{Bmatrix}$$

In this paper shear effects were not considered.

The inverse finite element method (iFEM) reconstructs the deformed structural shape due to a weighted least square functional Φ containing the strains acquired during data collection, e^{ε}, and *e(u)* defined by Eq. (2). The functional to minimize, as stated in Tessler and Spangler 2004 and Gherlone et al. 2014, was:

(7)
$$\Phi_e(u) = \left\| e(u) - e^{\varepsilon} \right\|^2 + \left\| k(u) - k^{\varepsilon} \right\|^2 + \lambda \left\| g(u) - g^{\varepsilon} \right\|^2$$

Considering each iTRIA3 with a specific area A_e , the squared norms were the following:

(8)
$$\left\| e(u) - e^{\varepsilon} \right\|^2 \equiv \frac{1}{n} \int_{A_e} \sum_{i=1}^{n} \left[e(u)_i - e_i^{\varepsilon} \right]^2 dx\, dy$$

$$\left\| k(u) - k^{\varepsilon} \right\|^2 \equiv \frac{(2t)^2}{n} \int_{A_e} \sum_{i=1}^{n} \left[k(u)_i - k_i^{\varepsilon} \right]^2 dx\, dy$$

$$\left\| g(u) - g^{\varepsilon} \right\|^2 \equiv \frac{1}{n} \int_{A_e} \sum_{i=1}^{n} \left[g(u)_i - g_i^{\varepsilon} \right]^2 dx\, dy \quad or \quad \left\| g(u) - g^{\varepsilon} \right\|^2 \equiv \frac{1}{n} \int_{A_e} g(u)^2\, dx\, dy$$

Where $n \geq 1$ was the number of strain gauge sensor locations in an iTRIA3 element domain, while $\lambda \geq 0$ (range of 10^{-5}-10^{-8}) was a scalar penalty parameter, which provide the appropriate coupling among the bending and the transverse shear terms. Whereas, the $(\bullet)^{\varepsilon}$ quantities represent the continuous "experimental" SGs measures.

The shear deformation was not considered, if the second form of the transverse shear ***g(u)*** norm was applied, referring to thin plate and shell structures Kirchoff Theory, 1850. Due to classical FEM (Zienkiewics), the displacements can be expressed with the *C^0-continuous* shape functions (linear function in *x* and *y*) matrix [**N**]. This was referred to the 2-D element (Figure 1), which is also called linear triangular element or constant strain triangle (CST).

$$\{u\} = [N]\{u_e\} \tag{9}$$

The strain-displacement relationship was given by:

$$\{e(u)\} = [B]\{u_e\} \tag{10}$$

$$[B] = \partial[N] \tag{11}$$

replacing Eq. (11) in Eq. (10):

$$\{e(u)\} = \partial[N]\{u_e\} \tag{12}$$

where **[B]** matrix, for a three node element, has the following form:

$$[B] = \frac{1}{2A_e}\begin{bmatrix} y_{23} & 0 & y_{31} & 0 & y_{12} & 0 \\ 0 & x_{32} & 0 & x_{13} & 0 & x_{21} \\ x_{32} & y_{23} & x_{13} & y_{31} & x_{21} & y_{12} \end{bmatrix} \tag{13}$$

$$\Phi^e(u) = \frac{A_e}{n}\sum_{i=1}^{n}\left[\varepsilon_i^e - \bar{\varepsilon}_i^e\right]^2 = \frac{A_e}{n}\sum_{i=1}^{n}\left[\left[B^e\right]\{u_e\} - \bar{\varepsilon}_i^e\right]^2 =$$
$$= \frac{A_e}{n}\sum_{i=1}^{n}\left[\left[B^e\right]\{u^e\} - \overline{\varepsilon_i^e}\right]^T\left[\left[B^e\right]\{u^e\} - \overline{\varepsilon_i^e}\right] = \tag{18}$$

considering the TRIA3 element area A_e as:

$$A_e = \frac{1}{2}\det\begin{bmatrix} 1 & x_1 & y_1 \\ 1 & x_2 & y_2 \\ 1 & x_3 & y_3 \end{bmatrix} \tag{14}$$

The notation $x_{ij}=x_i-x_j$ and $y_{ij}=y_i-y_j$ (*i, j= 1, 2, 3*). As stated in the introduction, the material and loads information were not required. But, if they were considered, it was possible to obtain the stiffness matrix **[K]** or the loads on the structure:

$$[K] = \int_V [B]^T[E][B]dV = 2tA_e([B]^T[E][B]) \tag{15}$$

Finally, the element force matrix {*F*} can also be readily computed:

$$[K]\{u_e\} = \{F\} \tag{16}$$

Overall process was computationally efficient because the method, so far described, was based on linear equations (ref. Eq. (9)).

In order to obtain the displacements field, in this work the case of pure traction was considered, so the functional to minimize Eq.(7) will be:

$$\Phi_e(u) = \left\| e(u) - e^{\varepsilon} \right\|^2 \tag{17}$$

For whole structure, composed by *n* elements:

$$= \frac{A_e}{n}\left\{\left\{u^e\right\}^T\left(\sum_{i=1}^{n}\left[B^e\right]^T\left[B^e\right]\right)\left\{u^e\right\} - 2\left\{u^e\right\}^T\left(\sum_{i=1}^{n}\left[B^e\right]^T\overline{\varepsilon_i^e}\right) + \left(\sum_{i=1}^{n}\left(\overline{\varepsilon_i^e}\right)^2\right)\right\}$$

Considering:

(19) $$\left[\mathrm{A}^e\right] = \frac{A_e}{n}\sum_{i=1}^{n}\left[B^e\right]^T\left[B^e\right]$$

(20) $$\left\{\beta^e\right\} = \frac{A_e}{n}\sum_{i=1}^{n}\left[B^e\right]^T\overline{\varepsilon_i^e}$$

(21) $$\gamma^e = \sum_{i=1}^{n}\left(\overline{\varepsilon_i^e}\right)^2$$

Where *q* was the displacement vector.

Replacing Eqs.(19),(20) and (21) in the Eq.(18) and minimizing $\partial\Phi/\partial\left\{u^e\right\} = 0$:

(22) $$[\mathrm{A}^e]\{u^e\} = \{\beta^e\}$$

(23) $$\{u^e\} = [\mathrm{A}^e]^{-1}\{\beta^e\}$$

So the displacement field was extracted thanks to the Eq.(23).

As stated in Tessler and Spangler 2004 the boundary conditions were defined on the two parts of the shell boundary surrounding the mid-plane (*t=0*).

Next sections describe in detail the test article tested in the structures laboratory.

3 TEST ARTICLE

3.1 DIRECT FEM

To have an accurate numerical solution, and a comparison, the direct FEM was considered. The analysis was performed thanks to the MSC/NASTRAN environment. The direct FEM study was carried out considering three different types of mesh refinements, using NASTRAN triangular elements (TRIA3), for evaluating the displacements. The first one, a fine mesh composed by 1280 TRIA3 elements and 693 nodes; the second one, a intermediate mesh (NASTRAN automatic suggested discretization), consider 56 elements and 40 nodes, the third one, consider only 24 elements and 21 associated nodes. A preliminary comparison (Table 2) confirms the differences between fine, intermediate and coarse mesh (e.g. experimental) produce an error < 1%, on maximum bending (w_{MAX}) value. These results suggest the low-fidelity mesh can also be utilized for the inverse formulation due to iTRIA3 elements, remembering that iTRIA3 has the same kinematic interpolation functions of TRIA3 (Zienkiewics 2000).

Table 2. Comparison on maximum bending of different plate discretization.

Mesh Type	**No. Elements**	**No. Nodes**	**Maximum bending (*w*) [mm]**
Fine	1280	693	1.0864394E+02
Intermediate (NASTRAN auto)	56	40	1.0814259E+02
Coarse (experimental)	24	21	1.0816554E+02
			Error <1%

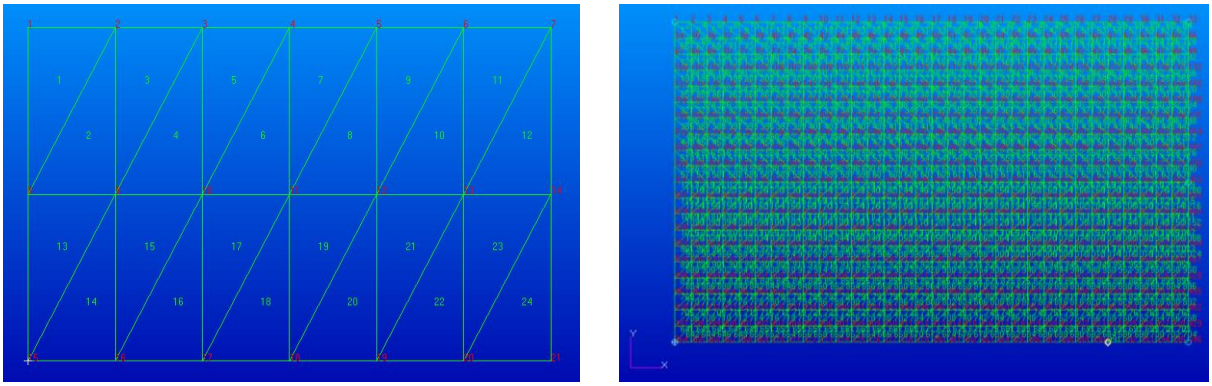

a) b)

Figure 3. a) Coarse mesh (experimental) used for strain gauge positioning and mounting, b) fine mesh (used for comparing).

Therefore, the coarse mesh configuration (experimental) was selected, as reference, for SGs positioning on the test article, for its simplicity and higher computational efficiency. The instrumented test article (Figure 4a) was an aluminum alloy plate (2024 T3) which measures 360 x 225 mm with a thickness of 2 mm. The test article was loaded as cantilever, clamped, on the test rig, by means 6 bolts at one side and vertically loaded on the other end (Figure 4).

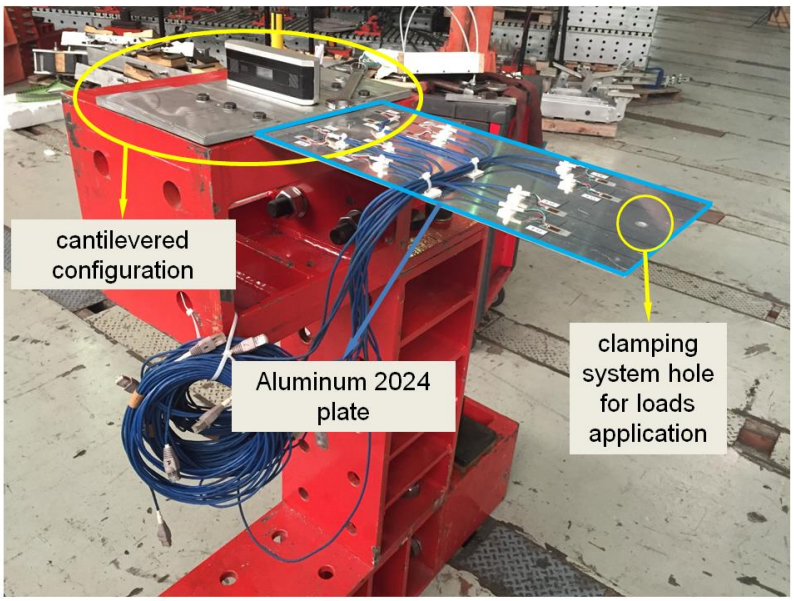

Figure 4. Test article, aluminum 2024 T3 and details of the test bench setup.

3.2 STRAIN GAUGES SETUP

For demonstrating the method estimation capability of structural displacements, strain gages were opportunely positioned on the test article.

According to the coarse mesh in Figure 4a, the positioning of the SG on top surface, was done. The SGs were centrally located with respect to the iTRIA3 element area (centroid). The iFEM model extracts displacements considering strains extracted during tests from strain gauge sensors, which were installed according to the scheme in Figure 6 and the Figure 4a (coarse mesh).

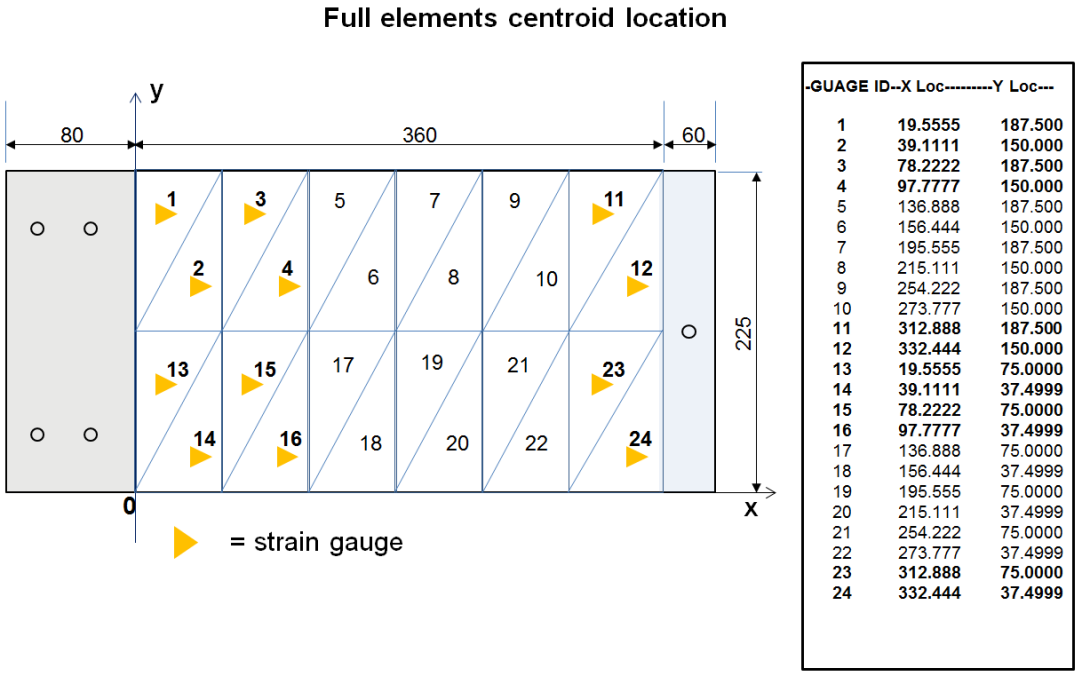

-GUAGE ID-	-X Loc---------	-Y Loc---
1	**19.5555**	**187.500**
2	**39.1111**	**150.000**
3	**78.2222**	**187.500**
4	**97.7777**	**150.000**
5	136.888	187.500
6	156.444	150.000
7	195.555	187.500
8	215.111	150.000
9	254.222	187.500
10	273.777	150.000
11	**312.888**	**187.500**
12	**332.444**	**150.000**
13	**19.5555**	**75.0000**
14	**39.1111**	**37.4999**
15	**78.2222**	**75.0000**
16	**97.7777**	**37.4999**
17	136.888	75.0000
18	156.444	37.4999
19	195.555	75.0000
20	215.111	37.4999
21	254.222	75.0000
22	273.777	37.4999
23	**312.888**	**75.0000**
24	**332.444**	**37.4999**

Figure 5. Scheme of the test article for strain gauge sensors positioning.

Not all elements were equipped with a SG sensor. They were positioned mainly near the clamp, where bending (strain-curvature) is max, vice versa the deflection will be close to zero. This latter assumption has been validated considering the *w* distribution between the strain gauges positioned on overall elements of the plate (24 elements – Full SG), and the strain gauges position of the scheme in Figure 6 (12 elements-Partial SG). The Figures 8a and 8b show the two cases previously described:

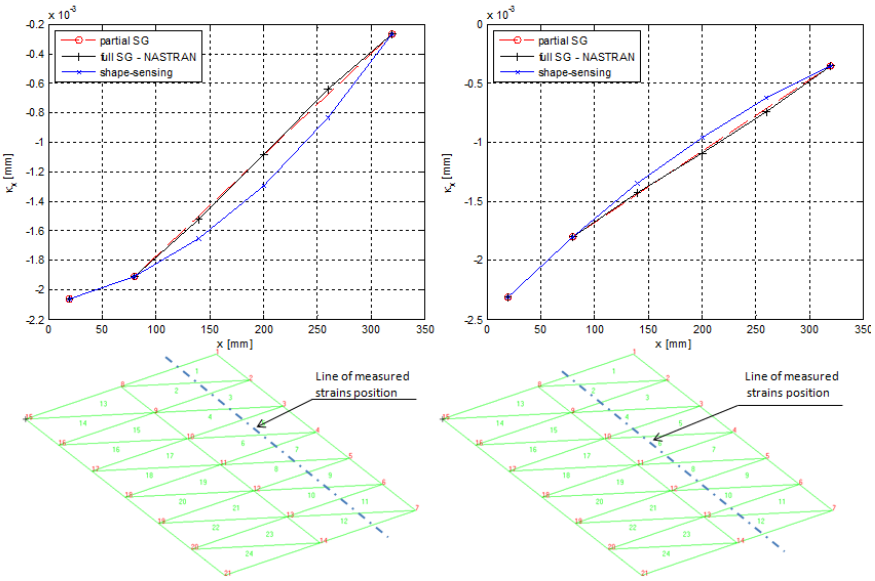

Figure 6. Strain interpolation due to a polynomial function (shape-sensing).

a) b)

Figure 7. a) partial SG (adopted for experimental session), b) Full SG.

The strain gauge sensors were represented by blue triangles, in Figures 8a and 8b above. The error on z-displacement (Table 3) was less than 1%, therefore, it was possible to consider only 12 SGs and extract the missing elements strain considering a polynomial function (shape-sensing) obtained from the known strains. In this case it was considered a *p(x)* of 2th order polynomial function (Kreyszig 1993) Eq.(24), for curvature reconstruction along the structure involved.

(24) $$p(x) = ax^2 + bx + c$$

Table 3. Strain-displacement comparison full/partial strain gauges on plate.

No. strain	w_{max} [mm]
24	108.2405
16	109.0840

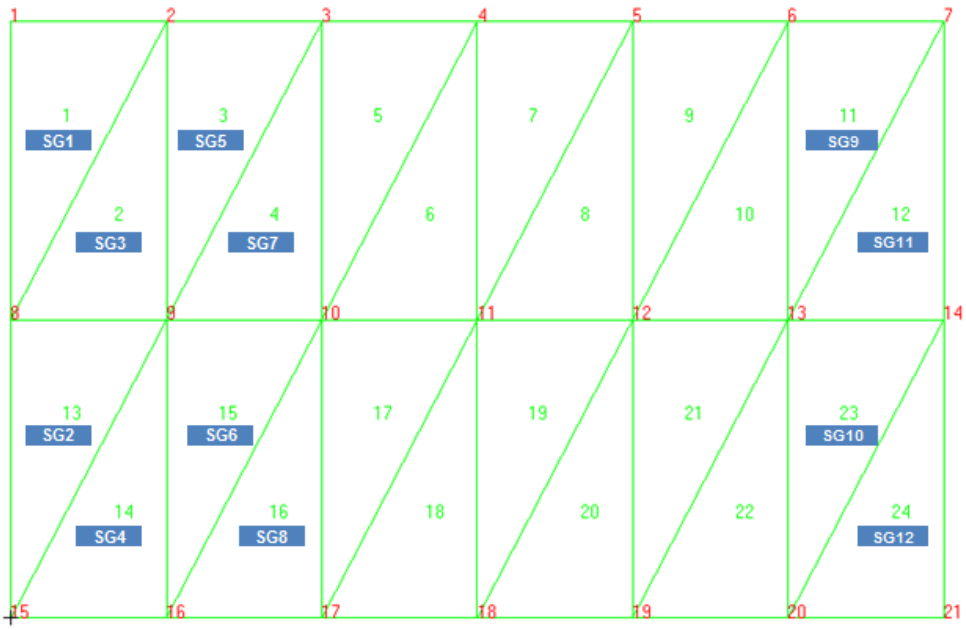

-Entity ID-	--X Location-	--Y Location-
1	19.5555	187.500
2	39.1111	150.000
3	78.2222	187.500
4	97.7777	150.000
5	136.888	187.500
6	156.444	150.000
7	195.555	187.500
8	215.111	150.000
9	254.222	187.500
10	273.777	150.000
11	312.888	187.500
12	332.444	150.000
13	19.5555	75.0000
14	39.1111	37.4999
15	78.2222	75.0000
16	97.7777	37.4999
17	136.888	75.0000
18	156.444	37.4999
19	195.555	75.0000
20	215.111	37.4999
21	254.222	75.0000
22	273.777	37.4999
23	312.888	75.0000
24	332.444	37.4999

Figure 8. Test article top view with SGs ID, mapping and locations.

The SGs were installed in the Airframe Laboratory of Leonardo Company, Figures 10b, 11a and 11b show the plate instrumentation, during various stages. The SGs utilized were CEA-13-250UW-350 (Figure 10a), universal general-purpose strain gauges with a strain range of 5%, gauge factor of 2.130, transverse sensitivity of 0.2, gauge resistance of 350 Ω and a temperature range from -75° to 175°C (-100° to 350°F) [15].

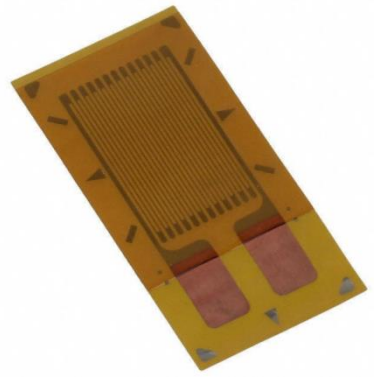

a)

b)

Figure 9. a) Strain gauge CEA-13-250UW-350. b) Structure cleanup with partial SG mounting.

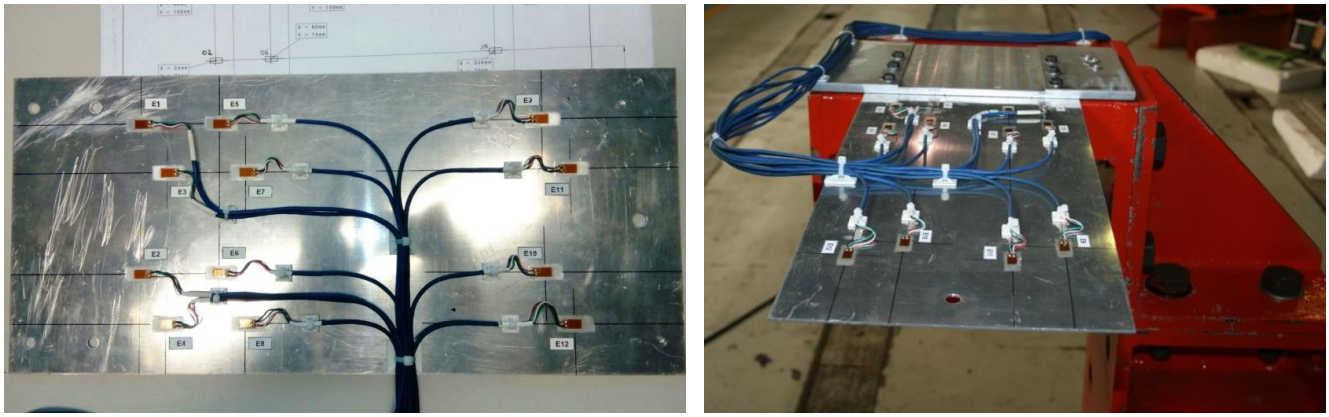

a) b)

Figure 10. a) Test article fully SG-equipped. b) test article mounted on the test bench.

4 EXPERIMENTAL RESULTS – FEM VS. IFEM

The experimental sessions were performed in the Airframe Laboratory of Leonardo Company in order to verify the effectiveness of the iFEM method. Various step of loads on the free end (tip) of the test article were considered and, in the same time, the strain measurements were acquired considering the equations considered in the section 2, the Figure 11 resume how the displacements field were extracted:

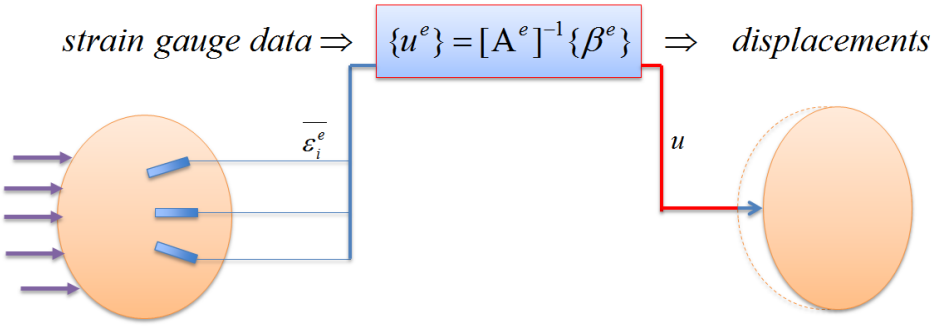

Figure 11. Displacements field extraction thanks to the iFEM.

The first condition consider the effects of the test article under its own weight, strain data were stored (Figure 13a).

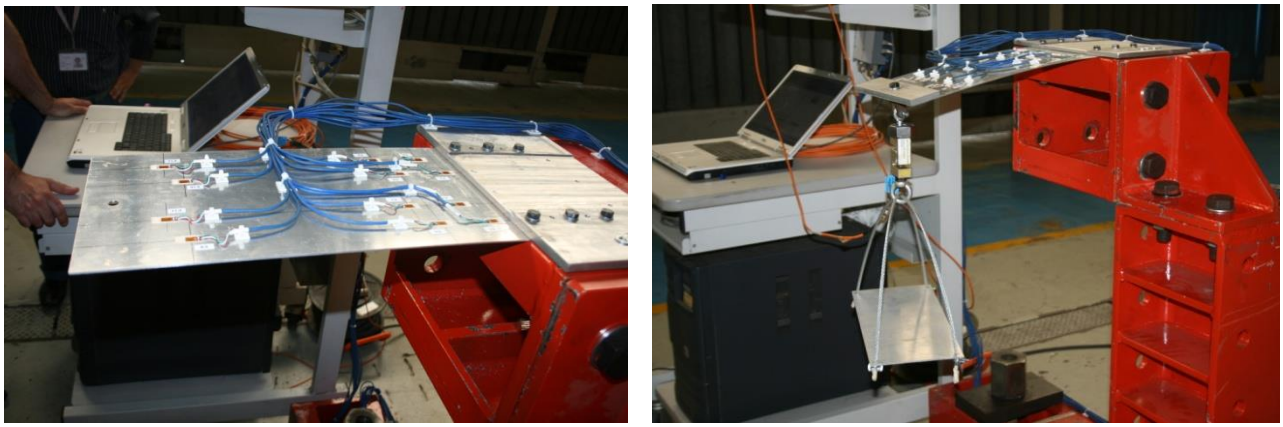

a) b)

Figure 12. a) Initial plate configuration, b) clamping system and container for weights.

The static loads were applied by means an aluminum basket (Figure 13b) which was able to contain the weights for each load step case. Table 4 shows the load case number, oriented like gravitational acceleration (*g*), and the measured deflection during test.

Table 4. Load cases on plate tip.

Load Case [N]	**Direction**
10	downward
20	downward
30	downward
40	downward
50	downward

The deflection *w* was obtained by integrating the rotations (ref. Eq. (4)) measured during the tests.

The LC (load case) data, from a load cell were measured.
Thus, it was possible to insert strain data measurements in the iFEM algorithm, extracting the z-displacements and comparing them with the FEM predicted z-displacements. Firstly a shape-sensing analysis was required, in manner to extract the missing strain data, where SG were not present.

The Figure 13 shows the known strain gauge data (black stars), in terms of curvature κ_x, the polynomial functions (red triangules), useful for strain interpolation (shape-sensing), and the comparison with NASTRAN strain data (blue circles). This, for each array of SGs from SG1 to SG12 (ref. Figure 9).

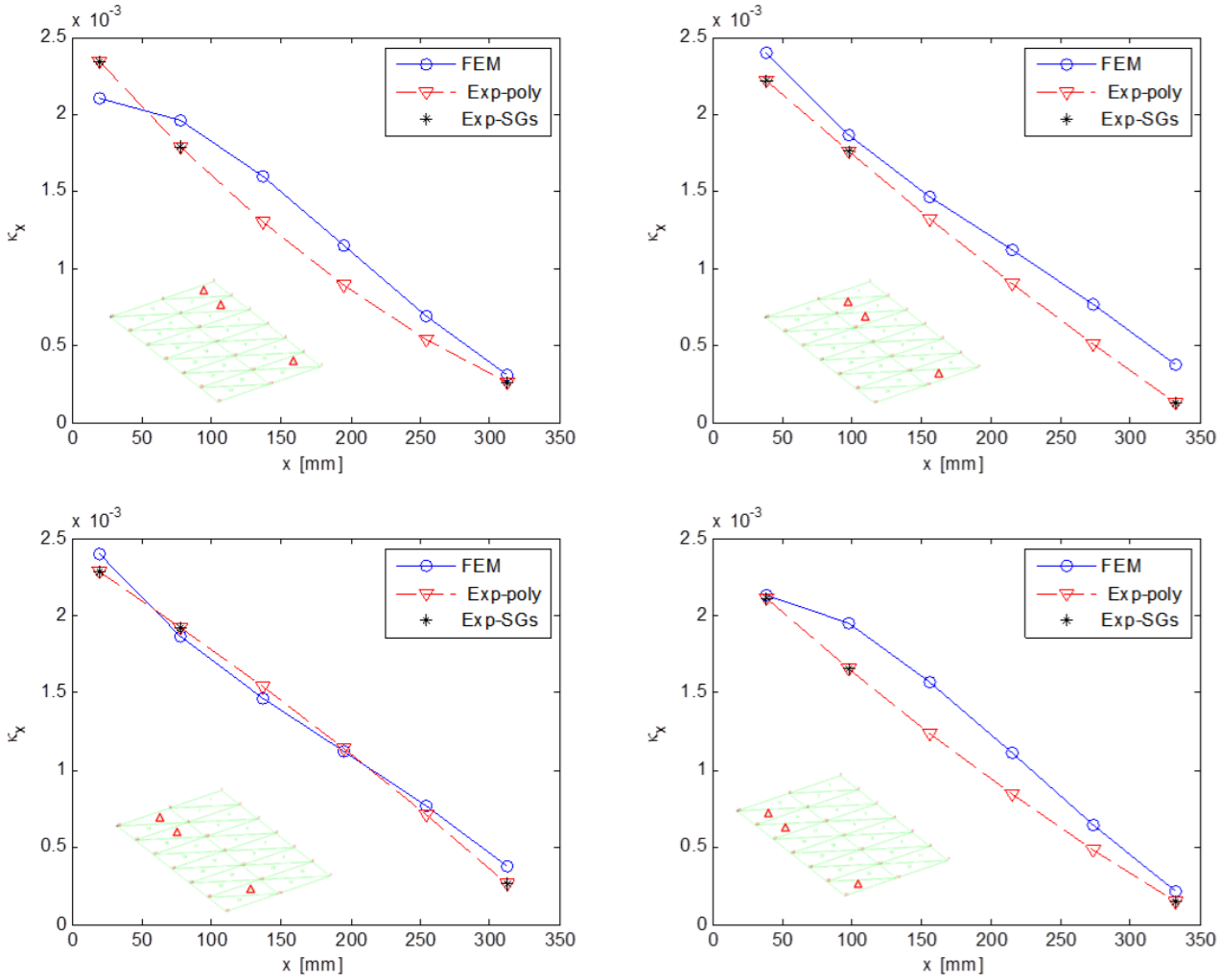

Figure 13. Shape sensing for 50 N step load and FEM (NASTRAN) comparison at various plate station.

The differences between the data acquired from SGs and the predicted from direct FEM were depicted in the Figure 13, confirming that the strains values were quite similar. The last step was to insert SGs data in iFEM algorithm and extract the plate z-displacements. The results were depicted in the Figure 14:

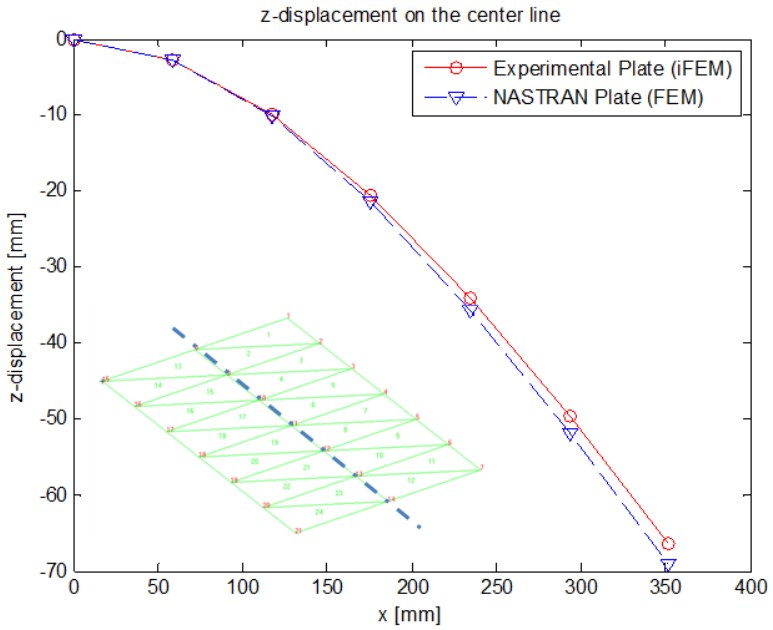

Figure 14. z-displacements on the center line comparison, direct (FEM) vs. inverse (iFEM).

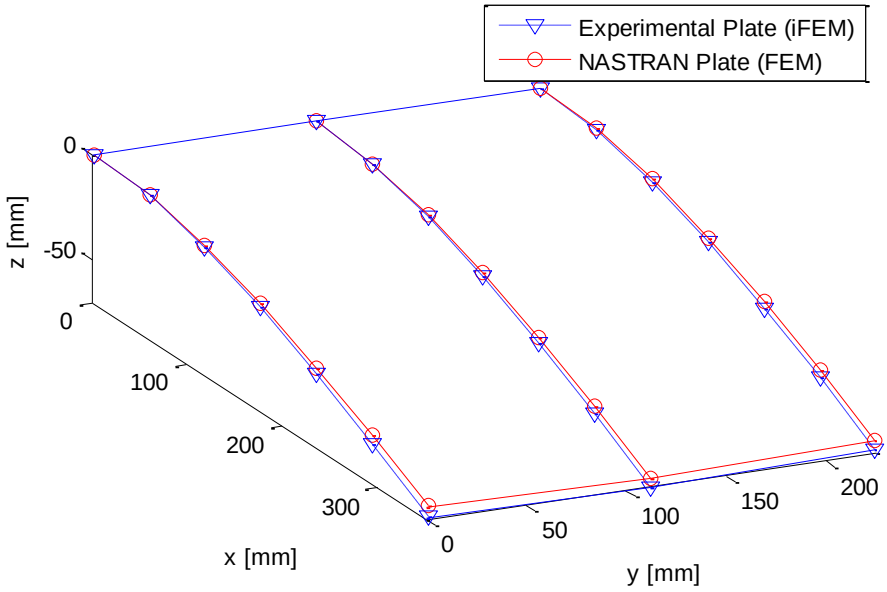

Figure 15. Overall plate z-displacements comparison, direct (FEM) vs. inverse (iFEM).

Considering the maximum z-displacement, considerations on the error was done, comparing the direct method with the inverse method. The Table 6 shows the maximum z-displacement and the error.

Table 6. FEM vs. iFEM error estimation.

Load-step [N]	Max z-displacement [mm]		Error [%]
(Load cell read)	**FEM**	**iFEM**	
20.91	-26.4442	-26.3962	0.18151
31.54	-40.0942	-39.8877	0.51504
41.96	-53.0655	-52.8295	0.44473
52.54	-65.3954	-66.4467	1.607605
63.28	-77.7033	-77.3323	1.47746
73.45	-92.8899	-89.0562	4.12714
84.50	-106.8645	-101.6750	4.85615

An error of about 4% on this type of analysis was acceptable.

5 CONCLUSIONS AND FURTHER WORKS

The full-field reconstruction of three-dimensional displacements from real-time strain measurements (i.e. *shape-sensing*), for an aluminum skin panel, has been validated, confirming a maximum error of about 4% between the direct FEM and iFEM on maximum deflection. This work, as previous (Papa et al., 2017), was fundamental and it has important implications for the aircraft design and monitoring of structural integrity.

As mentioned in the introduction, the iFEM has been applied to the shape-sensing of an aluminum 2024 plate for which experimental measurements were obtained in the Leonardo Company Airframe Structures Laboratory. A Mesh size sensibility and SG distribution have been analyzed in order to have a good accuracy of the predicted shape. Good correlations have been obtained through an equivalent plate configuration, of the skin fuselage, with a distribution of few strain gauge sensors on top surface of the skin.

Further works will point toward the opportunity of monitoring a full wing box configuration, landing gear structure during drop-tests, and also apply the iFEM in presence of torsion/combined loads, through the possibility of instrumenting the external and internal surfaces. Aims will be always focused on the structure health monitoring (SHM) for the airframe design and performance information systems.

REFERENCE

Bogert, P. B., Haugse, E. D., and Gehrki, R. E., 2003. Structural Shape Identification from Experimental Strains using a Modal Transformation Technique. Proceedings of 44th AIAA/ASME/ASCE/AHS Structures. Structural Dynamics, and Materials Conference, AIAA 2003-1626, Norfolk, Virginia.

CEA-06-250UW-350 Micro-Measurements. Datasheet, spec. general-purpose strain gauge, Document No.:11312, Revision: 25 Aug 2015.

Eisenbess, H., 2004. A Mini Unmanned Aerial Vehicle (UAV): System Overview and Image Acquisition. International workshop on *Processing and Visualization using High Resolution Imagery*, Institute for Geodesy and Photogrammetry, ETH, Zurich, CH.

Gherlone, M., Cerracchio, P., Mattone, M., Di Sciuva, M.,Tessler, A., 2014. An Inverse Finite Element Method for Beam Shape Sensing: Theoretical frame work and experimental validation, Smart Materials and Structures, vol. 23 no.4, 045027- ISSN 0964-1726.

Kreyszig, E.,1993. "*Advanced Engineering Mathematics*". John Wiley & Sons, seventh edition.

Noor, A. K., Venneri, S. L., Paul, D. B., & Hopkins, M. A., 2000. Structures technology for future aerospace systems. *Computers & Structures*, *74*(5), pp. 507-519.

Office of the Secretary of Defence, "*Unmanned Aircraft Systems Roadmap: 2005-2030*". Office of Secretary of Defence, Washington, DC, 2005.

Papa, U., Russo, S., Lamboglia, A., Del Core, G., & Iannuzzo, G. (2017). Health Structure Monitoring for the Design of

an Innovative UAS fixed wing through Inverse Finite Element Method (iFEM). Aerospace Science and Technology.

Shkarayev, S., Krashantisa, R., and Tessler, A., 2001. An Inverse Interpolation Method Utilizing In-Flight Strain Measurements for Determining Loads and Structural Response of Aerospace Vehicles. Proceedings of Third International Workshop on Structural Health Monitoring, Stanford, California, pp. 336-343.

Tichonov, A. N. and Arsenin, V.Y., 1977. " *Solution of Ill-Posed Problems".* Washington, DC: V. H. Winston and Sons.

Tarantola, A., 1987. " *Inverse Problem Theory: Methods for Data Fitting and Model Parameters Estimation*". New York: Elsevier.

Tessler, A. and Spangler, J. L., 2003. A Variational Principle for Reconstruction of Elastic Deformations in Shear Deformable Plates and Shells. NASA/TM-2003-212445, 2003.

Tessler, A., and Hughes, T. J. R., 1985. A Three-Node Mindlin Plate Element with Improved Transverse Shear. Computer Methods in Applied Mechanics and Engineering, Vol. 50, pp. 71-101.

Tessler, A., and Spangler, J.L., 2004. Inverse FEM for Full-Field Reconstruction of Elastic Deformations in Shear Deformable plates and Shell. NASA/TM-2004-0086696.

Tessler, A., Spangler, J.L., 2005. A least-squares variational method for full-field reconstruction of elastic deformations in shear-deformable plates and shells", Comput. Method Appl. Mech. Engrg, Vol. 194, pp. 327-339.

Zienkiewics, O.C., Taylor, R.L., 2000. "*The Finite Element Method – Vol.1: The Basis*", Fifth Ed., Butterworth – Heinemann.